Evolution of magnetotransport properties of Weyl semiconductor Te crystals with different Fermi energy

Cheng-Hao Yin,[1,2] Hong-Wei Fang,[3] Hong-Tao Jiang,[1,2] Lin Cao,[1,4] Shuang Han,[1,2] Yang-Yang Lv,[1,2,*] Jian Zhou,[1,4] Shu-Hua Yao,[1,4,†] Z. K. Liu,[3] Y. B. Chen,[1,2,‡] and Yan-Feng Chen[1,4,5]

[1]*National Laboratory of Solid State Microstructures, Nanjing University, Nanjing 210093, China*
[2]*Department of Physics, Nanjing University, Nanjing 210093, China*
[3]*School of Physical Science and Technology, ShanghaiTech University, Shanghai 201210, China*
[4]*Department of Materials Science and Engineering, Nanjing University, Nanjing 210093, China*
[5]*Collaborative Innovation Center of Advanced Microstructures, Nanjing University, Nanjing 210093, China*

(Received 28 March 2023; revised 5 September 2023; accepted 25 October 2023; published 13 November 2023)

The Weyl semiconductor is a type of semiconductor material that exhibits unique electronic properties. Tellurium (Te) is a recently discovered quantum material that exhibits quasilinear electronic dispersion, as opposed to the linear dispersion commonly observed in conventional Weyl semimetals. Its electrical- and magnetotransport properties, especially in Te crystals with different Fermi energy, have not been thoroughly investigated in prior studies. Here we successfully grew a series of Te crystals with varied Fermi energy through different temperature-cooling rates in the self-flux method, whose hole concentration can be adjusted from 10^{15} cm^{-3} to 10^{16} cm^{-3}. In the case of low hole-concentration (10^{15} cm^{-3}) Te crystals, temperature-dependent resistance shows abstract semiconductor-metal-semiconductor transition behavior with temperature varied. However, in the case of high carrier concentration, it demonstrates a transition from a semiconductor to a metallic state at a temperature T ($T\sim$ 50 K). Remarkably, the magnetoresistance (MR), under paralleled electric (E) and magnetic (B) fields ($E\|B$), evolves from dominant weak-antilocalization behavior in low hole-concentration samples to coexistence of weak-localization and chiral-anomaly effect in high hole-concentration ones. The dependences of coefficient C_W of chiral anomaly in Te crystals with different Fermi energy on misaligned angle θ between E and B, and T, were systematically analyzed. The band structure of Te and the presence of an electronic band tail resulting from high hole-concentration doping were verified using angle-resolved photoemission spectroscopy. This study quantitatively discusses the complex magnetotransport evolution of Te crystals with varying Fermi energy. The analysis is based on the impurity band and Berry curvature of Weyl points within this system. The research conducted contributes to the advancement of knowledge regarding the transport properties exhibited by Weyl semiconductors.

DOI: 10.1103/PhysRevB.108.195121

I. INTRODUCTION

The study of topological materials can be traced back to the discovery of graphene [1]. Graphene exhibits Dirac points and linear dispersion around these points. The electronic band structure and physical properties of the device have undergone comprehensive research and analysis [2]. Since then, researchers have discovered a series of topological materials such as topological insulators [3], Dirac and Weyl semimetals [4–10], type-II Dirac/Weyl semimetals, etc. Especially in Weyl semimetals, Weyl fermions, being still elusive after being long sought after in particle physics, have been discovered in condensed matter systems. Furthermore, the presence of certain topological characteristics in Weyl semimetals, such as the occurrence of pairs of positive and negative Weyl points and the divergence of Berry curvature at these points, gives rise to distinct physical phenomena. Notable examples include the emergence of Fermi arcs on the material's surface [11], the occurrence of negative magnetoresistance (MR) due to chiral-anomaly effect [12], and even-order high-harmonic generation [13].

A recent study utilizing first-principles calculations has made a prediction regarding the formation of Weyl points in the semiconductor material Te. This prediction is based on two key factors: the presence of a noncentrosymmetric crystal structure and a significant level of spin-orbit coupling (SOC). Additionally, Te is characterized by a narrow bandgap of approximately 0.32 eV [14], which was then verified by angle-resolved photoemission spectroscopy (ARPES) in experiment [15]. Subsequently, the spin momentum locking and a hedgehoglike radial spin texture in Te crystals are observed in experiments [16]. The unconventional spin polarization induced by Weyl fermions in Te crystals has been identified by researchers using ARPES experiments [17]. In the aspect of electrical-transport experiments, some works have reported the existence of negative longitudinal magnetoresistance and planar Hall effect in hole-doped Te crystals and it is nominated

*lvyangws0801@nju.edu.cn
†shyao@nju.edu.cn
‡ybchen@nju.edu.cn

as a *Weyl semiconductor* to distinguish it from a conventional Weyl semimetal [18]. The investigation of the evolution of the electrical-transport properties of Te at various Fermi energies was not conducted by them. Subsequently, certain researchers have made modifications to the Fermi energy and the intensity of chiral current through gating in Weyl semiconductor Te. This experimentation highlights the promising nature of Te as a highly effective material for topological phase change transistors [19]. And the logarithmic quantum oscillation is also observed in Te crystals, which may be caused by the formation of two-body quasibinding states between Weyl fermions with opposite topological charges [18,20,21]. Because Te has chirality and strong SOC, the complex magnetoconductivity behavior was then intensively studied by perturbation theory in a $\mathbf{k}\cdot\mathbf{p}$ model including SOC and Berry curvature effect [22,23]. Researchers have detected stronger spin polarization caused by the Edelstein effect in Te nanowires than those reported previously [24], and adjusted its amplitude in a wide range through electrical gating [24]. The transport transition from weak-antilocalization (WAL) to weak-localization (WL) effects caused by SOC was also detected in a two-dimensional (2D) Te layer through gating to tune its Fermi energy [25]. The following articles investigate the transport properties of nanowires and 2D Te samples using electric gating. The objective is to expand the range of Te-transport property manipulation. By intentionally introducing nonstoichiometry, we are able to examine the transport properties of Te crystals with varying Fermi energy levels, which correspond to different carrier concentrations. Scientifically, studying the evolution of transport properties of Te crystals under different Fermi energy may enrich our understanding of the Weyl semiconductors.

In consideration of the previously mentioned backgrounds, this study focuses on a systematic investigation of the electrical- and magnetotransport properties of Te crystals, which are Weyl semiconductors, with varying Fermi energy levels. The complex electrical and MR evolutions were observed when the Fermi energy was adjusted. The electronic band structure of Te and the presence of band-tail features were elucidated using ARPES. A proposed explanation for the complex evolution of transport properties in Te crystals is also presented, considering the potential physical mechanism involved.

II. EXPERIMENT AND METHOD

Te single crystal usually has self-doping characteristics, and it is easy to form hole-type semiconductors in the form of $Te_{1-\delta}$ [26]. The self-fluxing method is employed for the growth of high-quality Te single crystals. To begin, the high-purity Te powder (Alfa Aesar, 99.99%) is introduced into a quartz tube and subsequently sealed under vacuum conditions. After putting the quartz tube into a muffle furnace, we raise the temperature to 1000 °C, and then keep the temperature for 24 h to fully melt the Te powder. After that, the temperature is rapidly reduced to 900 °C at a speed of about 20 °C/h for the initial nucleation of the crystals, and then slowly cooled to 500 °C at a speed of about $2-8$ °C/h to grow crystals. After the furnace attained a temperature of 500 °C, the quartz tube underwent centrifugation in order to segregate the crystals from the flux. With the different growth rates, we have obtained a series of Te single crystals with varying hole concentrations. The crystal structure was determined by single crystal x-ray diffraction (XRD; Ultima III Rigaku X-ray diffractometer) with 2θ scanned from 10° to 90°. An energy-dispersive-spectroscopy (EDS) detector installed in a scanning electron microscope (FEI Inc., Quanta) was applied to characterize the chemical compositions of different Te crystals. The electrical- and magnetotransport measurements were conducted on the as-grown Te crystals using the standard six-electrode method. These measurements were performed in a 9 T physical property measurement system manufactured by Quantum Design.

ARPES measurements were performed at the beamline BL03U of Shanghai Synchrotron Radiation Facility (SSRF), China. The samples underwent *in situ* cleavage at a temperature of 17 K and were subsequently measured in an ultrahigh vacuum environment with a base pressure of less than 3.5×10^{-11} Torr. The photon energy of data acquisition for SSRF is 90 eV. Data was recorded by a Scienta R4000 at SSRF. The energy and momentum resolution were 10 meV and 0.2°, respectively.

The electron band structures and density of state (DOS) of Te are computed using the density functional theory method, which is implemented with the Vienna *ab initio* simulation package code [27,28]. The projected augmented-wave method [29,30] and the Perdew-Burke-Ernzerhof revised for solids exchange-correlation functional [31] are used in the calculations. The plane-wave cutoff energy is 260 eV and the k mesh is $9\times9\times6$ in the optimization and self-consistent calculations. The calculations of the DOS involve the utilization of a greater number of k points. The experimental lattice constants ($a=b=4.456$ Å and $c=5.921$ Å) [32] are used in the calculation but the atomic positions are optimized until the maximal residual forces on each atom are less than 0.01 eV/Å. In the band and DOS calculations, the spin-orbit coupling is included.

III. RESULTS

Figure 1 provides a comprehensive overview of the structural and compositional characterizations of as-grown Te crystals. The structure model of Te, as illustrated in Fig. 1(a), demonstrates the absence of inversion symmetry and instead features a chiral atomic chain composed of Te atoms. The typical XRD spectrum of the as-grown Te crystal, as depicted in Fig. 2, confirms the presence of high-quality single-crystalline Te crystals. The inset of Fig. 1(a) is the photograph of the four selected samples characterized in this work. Evidently, all samples have a metallic luster and their lengths can be as large as 1.5 cm. The scanning electron microscopy SEM image and the EDS mapping of the Te element [see Fig. 1(c)] corroborate the homogeneous elemental distribution in as-grown Te crystal. The EDS spectrum [see Fig. 1(d)] shows there are only characteristic peaks of the Te element in as-grown Te crystals. The data presented provides compelling evidence indicating that the as-grown Te crystals exhibit an exceptional crystalline quality and a consistent distribution of composition.

Figure 2 presents the electrical properties of four (S1–S4) typical Te crystals grown under different temperature-cooling

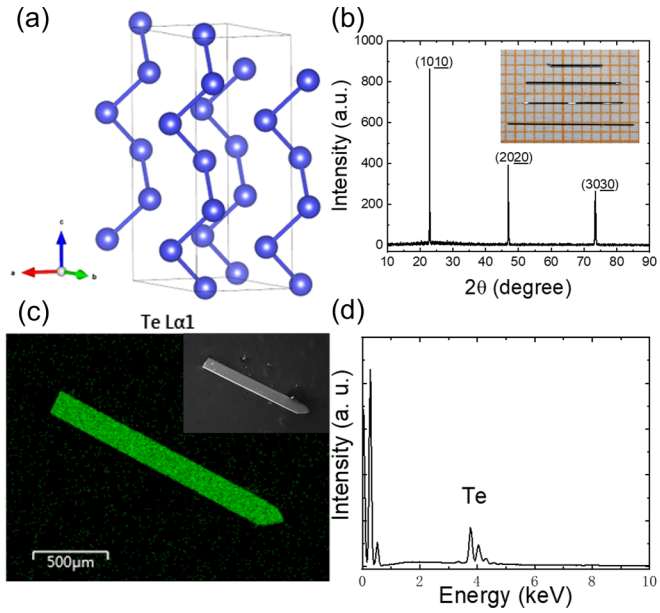

FIG. 1. (a) The atomic structure of a Te crystal without inversion symmetry. (b) The typical XRD data of as-grown Te crystals. The optical micrograph of the four samples characterized in this investigation is shown in the inset. (c) The EDS mapping (using the characteristic L peak of the Te element) of an as-grown Te crystal. The inset is the corresponding SEM image. (d) The EDS data of as-grown Te crystals.

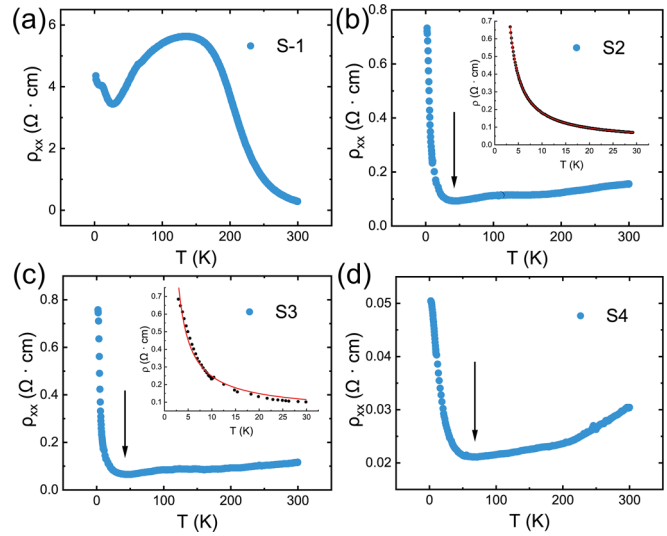

FIG. 2. (a)–(d) are the T-dependent resistance ρ_{xx} of the four samples (S1–S4) of Te crystals, respectively. The Fermi energies of S1–S4 are −0.2, −0.9, −1.0, and −2.2 meV, respectively, extracted from hole concentration (Fig. 3). The black arrows in (b)–(d) label the temperature of semiconductor-metal transitions. The insets of (b) and (c) are the fitting curves of these samples by using the variable-range-hopping model.

rates. Figures 2(a)–2(d) are the T-dependent resistance (ρ_{xx}) of four samples S1–S4 of Te crystals, respectively. The Fermi energy values for S1, S2, S3, and S4 are −0.2, −0.9, −1.0, and −2.2 meV, respectively. These values were obtained by extracting the hole concentration data from Fig. 3. Evidently, the resistance of S1–S4 Te crystals decreases dramatically when the Fermi energy is increased. Quantitatively, ρ_{xx} at 2 K of S1–S4 are 4.5, 0.7–0.8, and 0.05 Ω cm, respectively. In addition, one can see that the S1 sample shows the semiconductor feature ($d\rho_{xx}/dT < 0$) when $2\,\mathrm{K} < T < 25\,\mathrm{K}$; the metallic one ($d\rho_{xx}/dT > 0$) when $2\,\mathrm{K} < T < 150\,\mathrm{K}$; and the semiconductor feature again when $150\,\mathrm{K} < T < 300\,\mathrm{K}$. While the S2–S4 samples show simpler electrical-transport property, at low temperatures, the crystals demonstrate semiconductor features, and behave as metals at high temperatures. The temperature at which the semiconductor-metal transition occurs is indicated by black arrows in Figs. 2(b)–2(d). More quantitatively, we found that the ρ_{xx}-T curves of the S2 and S3 samples at low temperature range (2–30 K) can be well fitted by using the variable-range-hopping model, $\rho_{xx} = A\exp[(\frac{T_0}{T})^{1/4}]$ (where A and T_0 are two fitting parameters), as shown in the insets of Figs. 2(b) and 2(c). The strong concurrence observed between the experimental and fitting outcomes indicates that hole doping could potentially induce Anderson localization in the S2 and S3 Te samples when subjected to low temperatures.

The Hall data of crystals S1–S4 were measured, as shown in Figs. 3(a)–3(d). Obviously, the Hall resistivity ρ_{xy} of the S1–S4 samples almost linearly depends on B, especially when B is higher than 2 T. The slopes of ρ_{xy}-B lines are positive, showing typical hole carriers in these samples, and decrease from 2 to 300 K, suggesting that the hole concentrations are raised. The carrier concentrations and mobilities of the samples were determined quantitatively by analyzing the Hall resistance. This was done using the formula $\rho_{xx} = 1/ne\mu$ and $\rho_{xy} = B/ne$ (where μ, n, and e are mobility, hole concentration, and electronic charge, respectively). The results illustrated in Figs. 3(e)–3(h) demonstrate a gradual increase in hole concentrations from S1 to S4. And we calculate the Fermi energy E_F of each sample by using $E_F = \frac{\hbar^2}{2m^*}(3\pi^2 n)^{2/3}$ where m^* is the effective mass, which is $0.2m_e$, and $\hbar$ is the reduced Planck constant [33]. The E_F of S1–S4 are −0.2, −0.9, −1.0 meV, and −2.2 meV, respectively. In the calculation of E_F, hole concentrations measured at 20 K were used, and the top of the valance band is set as zero energy. The temperature-dependent mobility μ of S1–S4 shows the cusplike feature: initially, μ increases with T increased; then there is a μ peak, and then μ decreases when the T is further raised. The enhanced mobility observed at low temperatures can potentially be attributed to the disruption of Anderson localization caused by thermal excitation. Conversely, the reduced mobility observed at high temperatures can be attributed to the heightened occurrence of inelastic electron-phonon scattering [34].

The MR-B curves of S2–S4, under current $I \perp B$, T= 2, and 5 K, are shown in Fig. 4. The resistance of the S1 sample is too big to be measured in our experimental setup. The measurement configuration can be seen in the inset of Fig. 4(a). According to Fig. 4, the MR of S2 and S3 is greater than the MR of S4. The MR of S2/S3 is approximately 280% at a temperature of 2 K and 9 T. In comparison, the MR of S4 is approximately 80%. In addition, we found that the MR of S2–S4 can be well fitted by B^2 at low B regime (<5 T), which rules out the long-range-order magnetisms in hole-doped Te crystals (S1–S4). Otherwise, there should be negative MR [35].

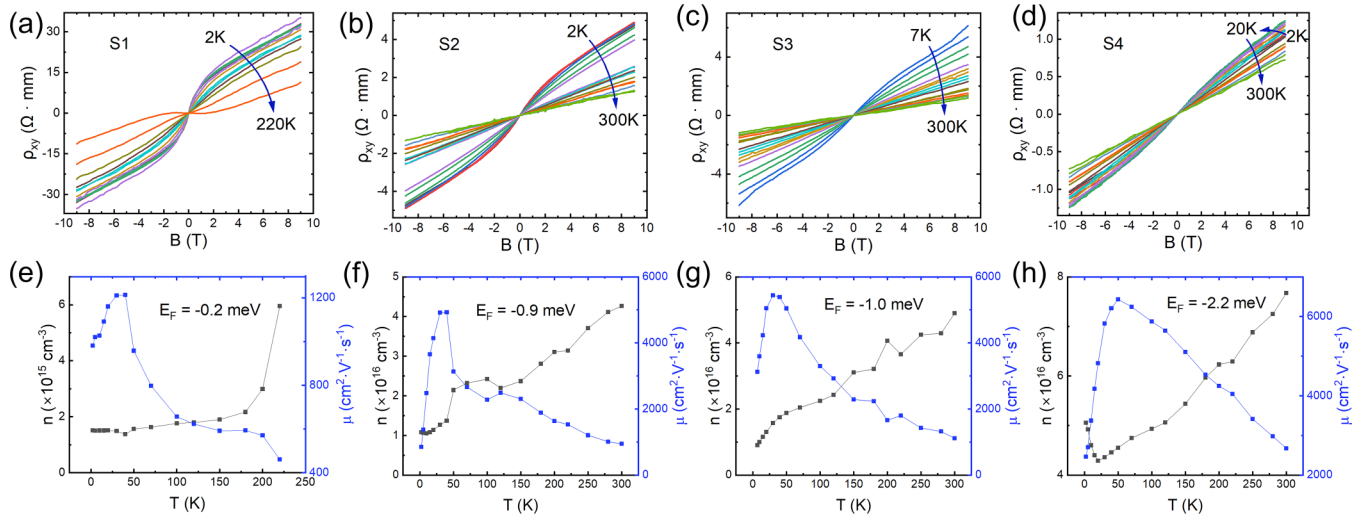

FIG. 3. (a)–(d) are the Hall resistance of the S1–S4 samples from 2 to 300 K, showing the dominated carrier of four samples is the holes. (e)–(h) are the temperature-dependent carrier concentrations and mobilities extracted from the Hall data. The Fermi energies of S1–S4 are −0.2, −0.9, −1.0, and −2.2 meV, respectively, calculated by means of hole concentration measured at 20 K. The top of the valance band is set as zero energy in the calculation of Fermi energy.

In order to study the effect of Weyl fermions in Weyl semiconductor Te, we conducted MR experiments by rotating B with respect to E at T= 2 K for the S1–S4 samples. The B was rotated from the crystal c axis to the direction of I, as shown in the inset of Fig. 5(a). The angle θ between E and B ranges from 0° to 90°. Figures 5(a)–5(d) show the MR curve at different angles θ of the S1–S4 samples, respectively. It is evident that the MR is highly sensitive to the angle θ. Qualitatively, the MR at low fields (<5 T) is changed from the apparent negative MR at $\theta = 0°$ to the fully positive MR behavior at $\theta = 90°$. When θ= 90°, the positive MR of the S2–S4 samples is roughly proportional to B^2 at low B regime ($B < 4$ T), which is the feature of Lorentz force. However, when $\theta = 0°$, complex MR behaviors are observed. Figures 5(e)–5(h) display an amplified MR plot of samples S1–S4, where the angle θ is set to 0°, within the low field range (<5 T), respectively. In S1, the curvature of MR is "V"-like, with the MR increasing with B raised. In S4, the MR decreases when B is increased, which is a "Λ"-like feature with a shoulder at 2 T. In S2 and S3, the MR demonstrates a complex evolution characterized by an increase in B.

In addition, a quantitative analysis was conducted on the MR data of samples S1–S4, as depicted in Figs. 5(e)–5(h). The initial analysis focused on the MR behaviors of the S1 and S4 samples due to their simplicity. The MR at different θ of S1 exhibits a $\sqrt{B}$-like feature in the range of 0–3 T whose fitting curvature is shown in Fig. 5(e), and this relationship is not sensitive to θ, suggesting that the WAL effect is dominant. The magnetoconductivity behavior of WL and WAL can be described by [36,37]

$$\Delta\sigma^{\mathrm{3D}}_{\mathrm{WL/WAL}} = C_{\mathrm{WL/WAL}} \frac{\sqrt{B}\cdot B^2 + \gamma B^2 B_c^2}{B^2 + B_c^2}, \qquad (1)$$

where $\Delta\sigma$ is the magnetoconductivity and B_c is the characteristic magnetic field ($B_c \sim \hbar/el^2_{\mathrm{WL/WAL}}$, $l_{\mathrm{WL/WAL}}$ is the mean free path of WL/WAL, respectively). $C_{\mathrm{WL}} > 0$ represents the WL effect while $C_{\mathrm{WAL}} < 0$ in the case of the WAL effect. As previously stated, the MR of S4 primarily consists of two main components: the WL effect and the chiral-anomaly effect. The formula for magnetoconductivity resulting from

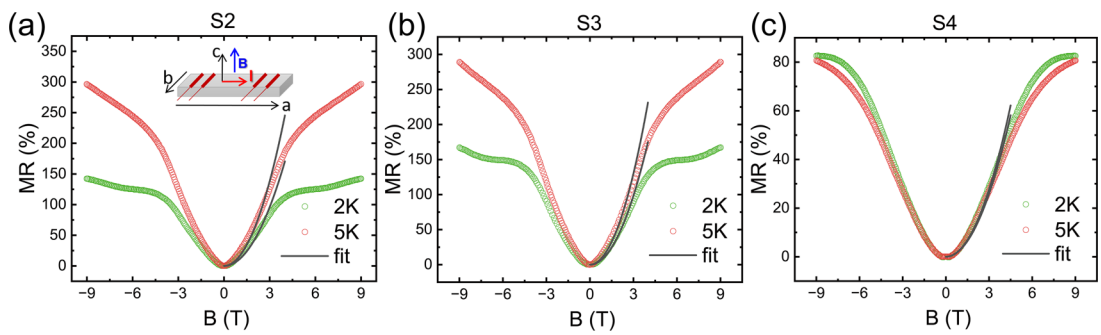

FIG. 4. (a)–(c) are the MR-B curves of the S2–S4 samples, under configuration as the current $I \perp B$ shown in the inset of (a), measured at low temperatures (2 and 5 K). At low B regime (<4 T), the MR is proportional to B^2, which rules out the long-range-order magnetism in as-grown Te crystals.

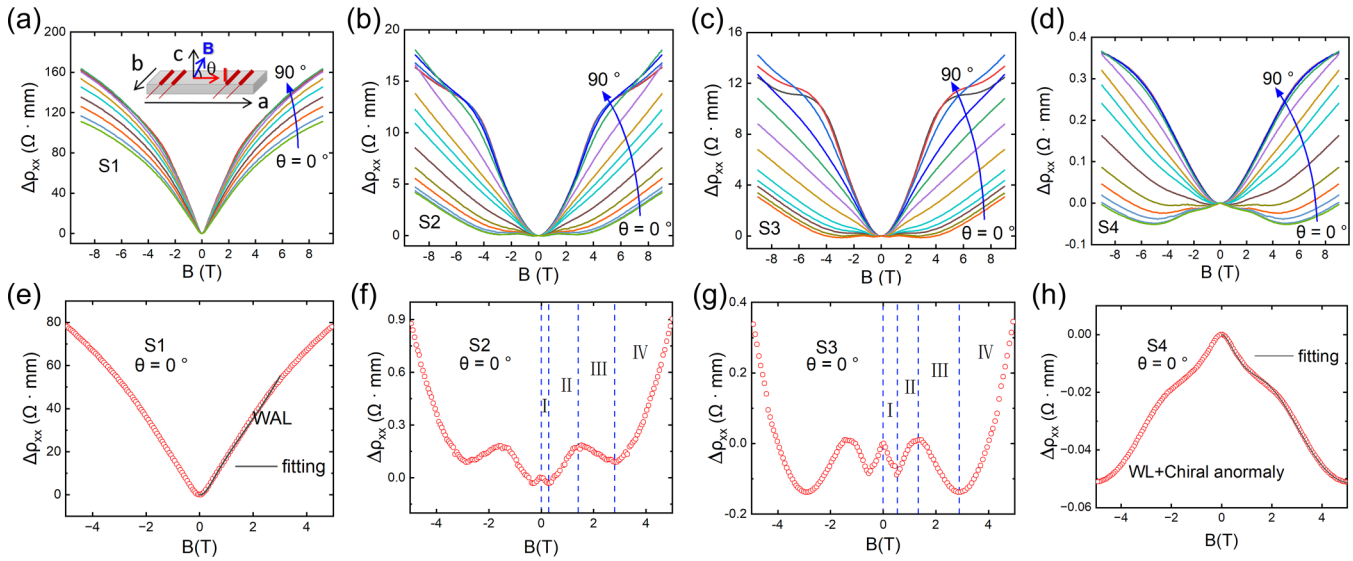

FIG. 5. (a)–(d) show the angle-θ dependent MR of the S1–S4 samples. θ is the angle between B and current I, which is shown in the inset of (a). When θ is changed from 90° to 0°, I changes from perpendicular to parallel to B. (e)–(h) show the details of MR curvatures at low B regime when θ is 0°. (f) and (g) show the complex MR evolution under B in samples S2 and S3, which could be divided into four regimes (I–IV); while S1 and S4 show quite simple MR behavior.

the chiral-anomaly effect is as follows [38]:

$$\sigma_C(B) = C_W B^2. \tag{2}$$

We used the sum of Eqs. (1) and (2) to fit the MR data of S4. As shown in Fig. 5(h), the MR data of S4 can be well fitted by Eqs. (1) and (2).

Next, a comprehensive analysis was conducted on the intricate MR behavior exhibited by S2 and S3. As depicted in Figs. 5(f) and 5(g), the MR can be partitioned into four distinct regions, each exhibiting a complex transitional behavior. Firstly, let us qualitatively discuss the MR behavior at regions I–IV. In region I, with the decreasing MR with B raised, it likely comes from the WL effect, while the rising trend MR in region II is mainly contributed by the WAL effect. And the decreased MR with B increase in region III is likely caused by the chiral-anomaly effect. In region IV, the magnitude of the B field is sufficiently large such that the dominant factor contributing to the positive MR is the Lorentz force. In summary, the previously mentioned intricate analysis of the evolution of magnetoconductivity in the S3/S4 samples can be condensed into a formula:

$$\sigma(B) = \Delta\sigma_{\mathrm{WL}}^{\mathrm{3D}} + \Delta\sigma_{\mathrm{WAL}}^{\mathrm{3D}} + \sigma_C + \sigma_L. \tag{3}$$

Using Eq. (3), we get a good fitting result of magnetoconductivity and take S3 as an example to show the details of each transport mechanism. Figures 6(a) and 6(b) show the fitting results and experimental magnetoconductivity of the S3 sample. These measurements were taken at $T = 2$ K and under varying θ. Additionally, the data collected at different T when θ is 0° is also presented. The contributions, from weak-localization, weak-antilocalization, and chiral-anomaly effects, to the measured magnetoconductivity of the S3 sample at 2 K and $\theta = 0°$ were separately shown in Fig. 6(c). Obviously, each magnetoconductivity item dominates at different B regions. Additional samples at different T and θ are presented in Figs. S1 and S2 in the Supplemental Material [39], and these results demonstrate that experimental results can be well fitted by Eq. (3).

Through these fitting parameters, we can quantitatively analyze the relationship between three kinds of relaxation time and T/θ in samples S1–S4. τ_{WL}, τ_{WAL}, and τ_t are relaxation time of weak localization, relaxation time of WAL, and transport relaxation time. τ_{WL} and τ_{WAL} can be extracted through $\tau_{\mathrm{WL/WAL}} = \frac{l_{\mathrm{WL/WAL}}}{v_F}$. Figure 7 shows the temperature-dependent τ_{WL}, τ_{WAL}, and τ_t. According to Fig. 7, there exist two distinct features. Firstly, at a low temperature, $\tau_{\mathrm{WL/WAL}}$ and τ_t is comparable where we can clearly observe the WL and WAL effects in the MR-B curves of the S2 and S3 samples. Secondly, with the rising of T, $\tau_{\mathrm{WL/WAL}}$ is gradually decreased because the coherence of electron wave is disrupted by thermal fluctuations; while at the same temperature range, transport lifetime τ_t is increased with T raised, which may come from the Anderson localization diminished by thermal agitation [38,40].

We also extracted C_W of the S2–S4 samples at different T and θ. The relationship between the C_W of the S2–S4 samples and the angle θ is shown in Figs. 8(a)–8(c), respectively. It is evident that when the direction of B diverges from E, there is a significant decrease in C_W, which aligns with the observed chiral-anomaly effect in Weyl semimetals [18]. We also studied the relationships between C_W of the S2–S4 samples and T, which is shown in Figs. 8(d)–8(f). Evidently, C_W of S2–S4 is decreased with T raised, which comes from the loss of electron coherence due to thermal perturbation. This trend is also observed in Weyl semimetals [41]. Quantitatively, the dependence between C_W and T can be written as [18]

$$C_W \propto \frac{v_F^3 \tau_v}{T^2 + \frac{E_F^2}{\pi^2}}, \tag{4}$$

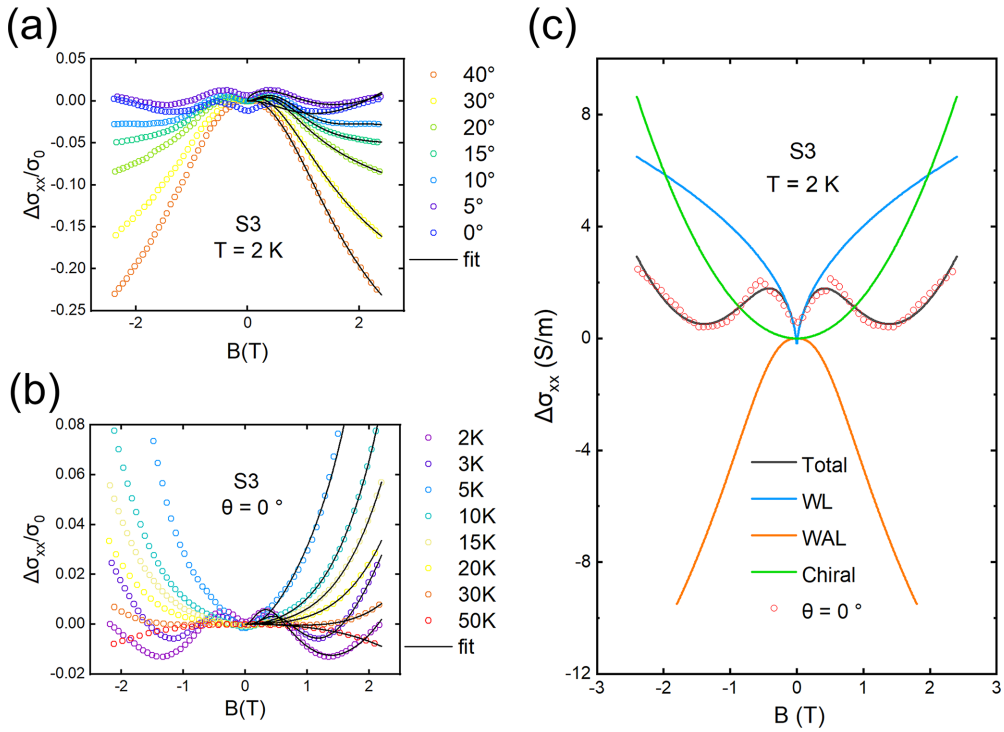

FIG. 6. (a) and (b) are the fitting and experimental magnetoconductivity results of the S3 sample under different θ at 2 K and at different T when θ is 0°, respectively. (c) The magnetoconductivity contributions to the measured magnetoconductivity of the S3 samples come from the different mechanisms (WL, WAL, and chiral-anomaly effect). Details can be seen in the main text.

where v_F and τ_v are Fermi velocity and chirality-changing scattering time. The theoretical curves of C_W of the S2–S4 samples are shown in the orange dashed lines in Figs. 8(d)–8(f). One can see that experimental data can be well fitted by Eq. (4).

In our endeavor, we made an attempt to extract spectroscopic data using ARPES of the Te samples. Figure 9(a) presents a comparison between the experimental electronic band structure of the S1 sample and its corresponding theoretical counterpart. It is evident that the theoretical framework effectively captures the comprehensive characteristics of the experimental electronic band structure. The profile of the electronic band structure and the position of the Weyl points along the *L*-*H* point of *k* space in our results are quite similar to those in a previous work [18]. However, another ARPES experiment and first-principles calculation substantiated that there are other Weyl points in the *H*-*K* direction and the Γ-*A* direction in the valence band of Te, as well as some Weyl points have chiral charges larger than 1 [17]. It is important to note that the Weyl points observed in our ARPES data [refer to Fig. 9(a)] exhibit a lesser degree of penetration into the valence band compared to the aforementioned magnetotransport data.

Figure 9(b) compares the integrated density of state of the S1 and S4 samples; evidently, the DOS around E_F declines more sharply in S1, while the DOS in S4 samples decreases more softly and generates a band tail extended to the band gap, which comes from the high hole-concentration doping. The theoretical DOS of the perfect Te is utilized in this study. A

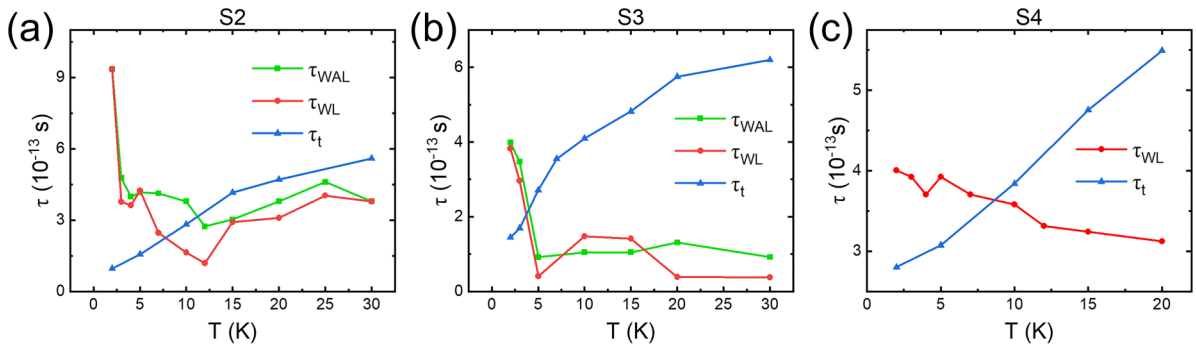

FIG. 7. (a)–(c) are the relationships between temperature and the experimentally extracted relaxation time of weak localization, τ_{WL}, the relaxation time of weak antilocalization, τ_{WAL}, and the transport relaxation time, τ_t, of the S2–S4 samples, respectively.

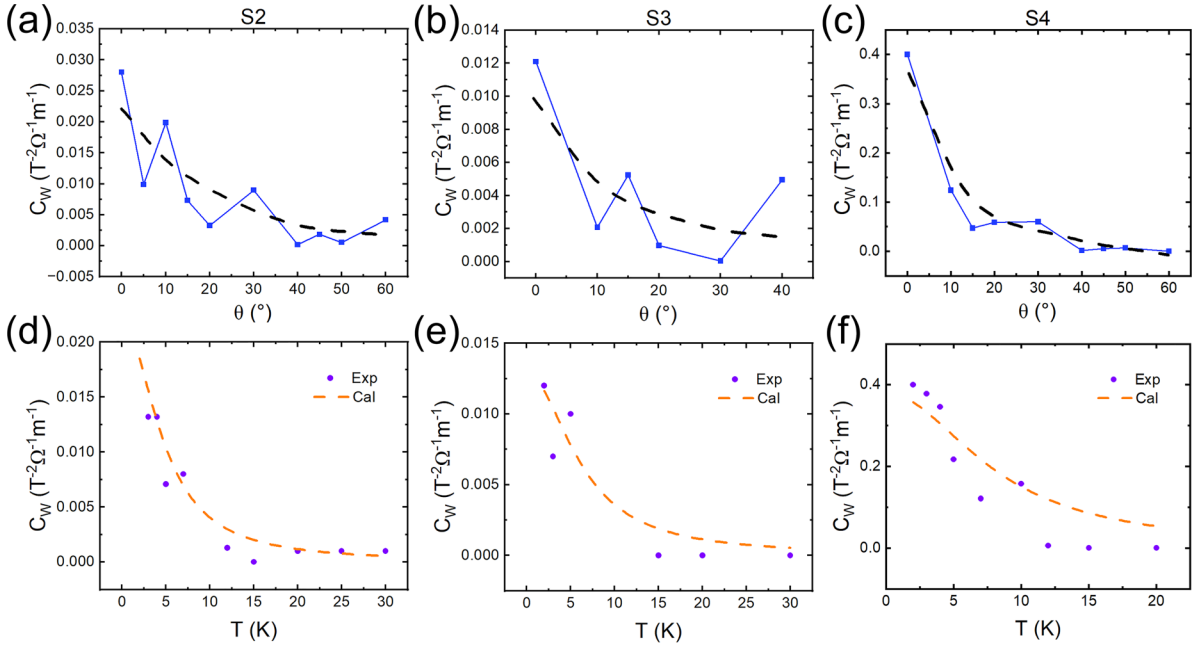

FIG. 8. (a)–(c) are the relationships between C_W and angle θ between E and B of the S2–S4 samples, respectively. Obviously, the C_W of the S4 sample is much larger than that of the S2 and S3 samples. (d)–(f) shows the dependence of C_W on T of the S2–S4 samples, respectively. Light-orange dashed lines are theoretical fitting results.

theoretical model is employed, where electrons are assumed to move in a Lorentzian random field with "white-noise" correlation. The DOS of the S1 and S4 samples is fitted using the following formula [42,43]:

$$g_{S1/S4}(\varepsilon) = \int_{-\infty}^{\varepsilon} g_{CAL}(\varepsilon - v)A(v)dv, \tag{5}$$

$$A(\varepsilon) = \frac{1}{\pi}\frac{\gamma_p}{(\varepsilon - \varepsilon_0)^2 + \gamma_p^2}, \tag{6}$$

where $g_{CAL}(\varepsilon)$ and $A(\varepsilon)$ are the theoretical DOS and a simple Lorentzian function with the width γ_p, respectively. The model is considered to have random elastic scattering impurity in crystals [42,43]. According to the fitting result, we can get the quasiparticle lifetime τ_φ ($\tau_\varphi = \frac{\hbar}{2\gamma_p}$) of the S1 and S4 samples that are 1.4×10^{-13} s and 6.9×10^{-14} s, respectively. The quasiparticle lifetime of the S4 sample is one order shorter than that of the S1 sample. This discrepancy arises due to the high impurity-scattering rate observed in heavily doped Te samples [42]. The presence of a short quasiparticle lifetime in the S4 sample results in a more pronounced band-tail feature [42,43].

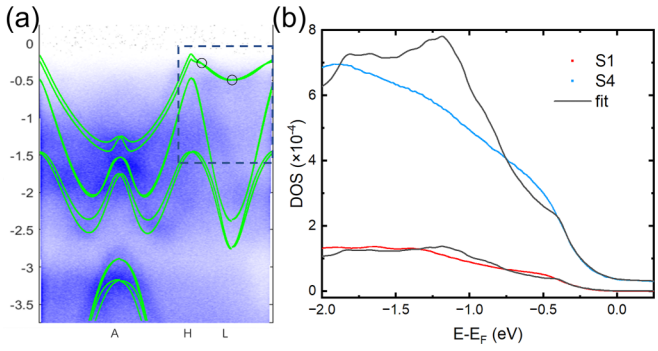

FIG. 9. (a) is the comparison of the theoretical electronic band structure and the ARPES data of the S1 sample. (b) is the experimental DOS at the top of the valence band of the S1 and S4 samples, as well as the fitting results by using the band-tail model.

IV. DISCUSSION

In this study, we present a preliminary explanation for the intricate changes observed in electrical resistance and magnetotransport as the Fermi energy is raised from the uppermost point of the valence bands. Please refer to Figs. 2 and 5 for visual representations of these phenomena. The simplified density of state and electronic band of doped Weyl semiconductor Te are depicted in Fig. 9. Except for the conventional valence band, we assume there is an impurity band created by Te vacancies. The presence of the impurity band is a widely observed phenomenon in both semiconductors and topological insulators [44]. Based on this toy model, we can understand the evolutions of electric and magnetotransport behaviors from S1 to S4 samples.

In the S1 sample, when the hole concentration reaches its lowest value of 1.5×10^{15} cm^{-3}, it is possible for the Fermi energy to become pinned around the impurity band. In this particular scenario, the presence of significant spin-orbit coupling within the Te element leads to the observation of WAL in MR. Additionally, the resistance at low temperatures does not exhibit the characteristic behavior of Anderson localization, specifically Mott variable range hopping. These features are coincident to experimental observations [see Figs. 2(a) and 5(e)].

When there are more holes in the S2/S3 samples (10^{16} cm^{-3}), Fermi energy may lie between the impurity band and the valence band. In this scenario, the electrical transport is influenced by the presence of electrons in the impurity band

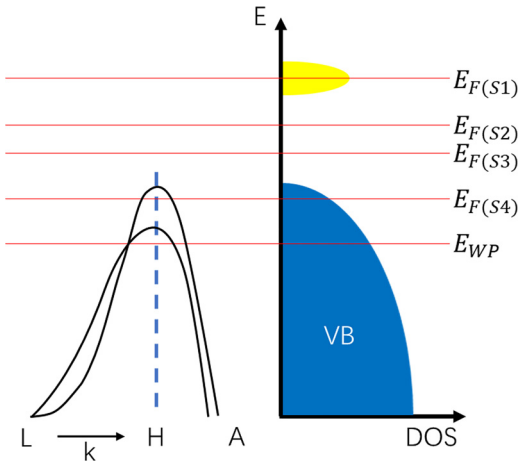

FIG. 10. The schematics of our toy model of the hole-doped Weyl semiconductor Te include an impurity band (the yellow region) and a valence band (the blue region) with Weyl points of Weyl semiconductor Te. The positions of the different Fermi energy of the S1–S4 samples and the Weyl points are marked respectively.

and holes in the valence band of Te. Typically, the dominant factor contributing to resistance is the presence of holes in the Te band. The electrons at the top of valence bands are easily formed in the Anderson localization state because of low Fermi velocity and high density of state [42]. Therefore, we expect to observe Mott variable range hopping in ρ_{xx}-T curves and negative MR, which fit the experimental data [see Figs. 2(b) and 2(c), insets]. However, it is important to note that the valence band of the Weyl semiconductor Te exhibits Berry curvature. Although the separation between the Fermi energy and the Weyl points is slightly significant (as indicated by the label in Fig. 10), the chiral-anomaly effect, when subjected to parallel E and B, results in a negative MR. This phenomenon has been observed in experimental data, specifically in regime III as shown in Figs. 5(f) and 5(g). In addition, similar to the S1 sample, the electrons at impurity bands have WAL effect due to SOC. Therefore, competition of WL, WAL, and chiral-anomaly effects leads to the complex MR behavior of the S2 and S3 samples [see Figs. 5(f) and 5(g) and Fig. 6(c)]. The determination of the dominant effect in a specific magnetic-field region necessitates rigorous numerical calculations.

The S4 sample has the highest hole concentration (4.3×10^{16} cm^{-3}); maybe the Fermi energy penetrates the valence band of Te. Similar to the S2 and S3 samples, the electrical conductivity is influenced by both electrons in impurity and holes at the valence band of Te. But in S4, the holes at the valence band of Te may be dominated by the transport behavior. Principally, the Anderson insulator feature and weak localization broken by magnetic field are under expectation in the S4 sample, which are also in line with the experimental data [see Fig. 5(h)]. Similar to the S2/S3 phenomenon, the presence of Weyl points near H points leads to an increased Berry curvature. As a result, we observe a negative MR effect, specifically due to the chiral-anomaly effect, when B is parallel to E. This can be seen in Fig. 5(h). And because Fermi energy penetrates deeply in the valence band, the distance between the Fermi energy and Weyl points is much closer than that of the S2/S3 samples. Therefore, C_W is largest among the S2–S4 samples, agreeing with experimental observation [see Figs. 8(d)–8(f)]. In this analysis, we utilize a simplified model that incorporates impurity bands to examine the behavior of electronic bands in Te. By considering the position of the Fermi energy and the Berry curvature, we can provide a logical explanation for the intricate electrical conductivity and magnetotransport phenomena observed in Te crystals when the Fermi energy is shifted.

Furthermore, we quantitatively discuss why the magnetotransport behavior evolves from WAL in the S1 sample to the coexistence of WL and chiral anomaly in the S4 sample, when the Fermi energy is more deeply penetrated into valence bands of Te. WAL in the S1 sample comes from spin-orbit coupling in Te. The major problem is in the S4 sample: theoretically, chiral anomaly normally coexists with WAL because Weyl points provide the electronic chirality and nontrivial π-Berry phase in Weyl semimetals. But how does the WL coexist with chiral anomaly in the S4 sample?

This section examines the simultaneous occurrence of chiral anomaly and WL in the Weyl semiconductor Te. Firstly, we will examine the chiral-anomaly effect observed in the S4 sample. The chemical potential of an electron with plus chirality is higher than that of an electron with minus chirality, as indicated by the parallel E and B fields. Mathematically, the particle number difference rate between plus chirality (n_+) and minus chirality (n_-), under $E\|B$, can be written as $\frac{\partial(n_+ - n_-)}{\partial t} = \frac{e^2}{2\pi^2\hbar^2}\vec{E}\cdot\vec{B}$ [45]. The different plus-chirality and minus-chirality electronic number leads to the different chemical potential. As a consequence, the presence of varying chemical potential can give rise to an additional current that is equivalent to a negative MR. The manifestation of this phenomenon becomes more prominent when the Fermi energy is in close proximity to Weyl points, which have been experimentally detected [46,47].

Secondly, we discuss why the WL can be observed in the S4 sample. According to maximally crossed diagrams in multiple scattering of electronic transport theory, the backscattering cooperon has the form of $\Gamma_{k_1,\,k_2} \approx \frac{\hbar}{2\pi N_F \tau^2}\frac{1}{Dq^2}e^{i(\varphi_2-\varphi_1)}$ [48], where $\varphi_2 - \varphi_1$ is the Berry phase γ; and N_F, τ, D, and q are the density of states, momentum relaxation time, diffusion coefficient, and cooperon wave vector, respectively. Therefore, the Berry phase γ being π or 2π completely determines whether systems demonstrate WAL or WL [48] after multiple scattering. As shown in Fig. 9(a), one can see that the electronic band structure of Te crystals is significantly deviated from the linear dispersion. The Berry phase around the Weyl points was quantitatively calculated in order to analyze the magnetotransport behavior in the S4 sample. Considering a Hamiltonian up to the perturbation of wave vector k^2 with the form of [48,49]

$$H = v\begin{pmatrix} k_z + c_2k_z^2 & k_- + c_1k_+^2 \\ k_+ + c_1k_-^2 & -k_z - c_2k_z^2 \end{pmatrix}, \tag{7}$$

we can then get an approximate eigenvalue $E(\vec{k}) = \pm v|\vec{k}| + vc_1\frac{k_x^3 - 3k_xk_y^2}{|\vec{k}|} + vc_2\frac{k_z^3}{|\vec{k}|}$, where $|\vec{k}| = \sqrt{k_x^2 + k_y^2 + k_z^2}$, v, c_1, and c_2 are parameters. The electronic band near the Weyl point

was fitted using Eq. (7) based on the results obtained from the first-principles calculation. The electronic band structures near Weyl points, as depicted in Fig. S3 of the Supplemental Material, exhibit a remarkable agreement with the effective Hamiltonian model (7) obtained from first-principles calculations. This agreement holds true over a wide energy range.

When the wrapping effect in the electronic band structure of Te is considered, the Berry phase γ is significantly deviated from π. Using the wavefunction of Eq. (7), we can get the final form of Berry phase $\gamma = \pm\pi(1 + \frac{1}{8}c_1|\vec{k}|\sin 3\theta) = \pm\pi(1 + \frac{1}{8}c_1|\vec{k}|\frac{3k_x^2 k_y - k_y^3}{(k_x^2+k_y^2)^{3/2}})$. Quantitatively, when $E_F = -0.127$ eV (simulating the Fermi energy of sample S4), the average of the calculated Berry phase γ is about $1.2 \times \pi$ that is significantly deviated from π. Hence, it is logically justifiable to anticipate that the channel of WL can be activated if the wrapping effect in the electronic band structure is prominent. Therefore, one can observe the coexistence of chiral anomaly and WL in the S4 Te sample. In a word, the WL of the S4 sample comes from the significant deviation of linear dispersion of electronic band structure when the Fermi energy is a little far away from the Weyl point. Different from the previous works [24,25], we observed the evolution from WAL to WL and chiral-anomaly effect in Te crystals when the Fermi energy is deeply penetrated into the valence bands, as well as quantitatively discussed the magnetotransport evolution by quantum transport theory.

V. CONCLUSION

We have successfully grown various Weyl semiconductor Te crystals with different Fermi energy by employing diverse growth-cooling rates. When Fermi energy is the lowest, the resistance-temperature curve shows the semiconductor-metal-semiconductor evolution, and MR is a simple WAL behavior; in intermediate Fermi energy, the resistance-temperature curve has the semiconductor-metal-transition, and MR shows WL, WAL, and chiral-anomaly behaviors. In the scenario where the Fermi energy is at its maximum value, the resistance-temperature curve exhibits a transition from a semiconductor to a metal state. Additionally, the MR shows WAL and chiral-anomaly features. These complex electrical- and magnetotransport evolutions in Te crystals with different Fermi energy can be rationalized by a toy model considering the impurity band and valence band of Te, the position of the Fermi energy, and the Berry curvature in the electronic band of Te. The quantum transport theory provides a quantitative analysis of the evolution of the magnetotransport mechanism, specifically from weak antilocalization to the coexistence of weak localization and chiral anomaly. This study holds potential value in elucidating the physical properties of Weyl semiconductors.

ACKNOWLEDGMENTS

We wish to acknowledge the financial support from the Foundation for Innovative Research Groups of the National Natural Science Foundation of China (Grant No. 51721001), and the National Natural Science Foundation of China (Grants No. 52272002, No. 51902152, No. 11874210, No. 11974163, No. 11890702, and No. 51890861). We thank Hao Geng at Nanjing University for his enlightening discussions about quantum transport theory.

[1] K. S. Novoselov, A. K. Geim, S. V. Morozov, D. Jiang, Y. Zhang, S. V. Dubonos, I. V. Grigorieva, and A. A. Firsov, Science **306**, 666 (2004).
[2] A. H. Castro Neto, F. Guinea, N. M. R. Peres, K. S. Novoselov, and A. K. Geim, Rev. Mod. Phys. **81**, 109 (2009).
[3] Y. Xia, D. Qian, D. Hsieh, L. Wray, A. Pal, H. Lin, A. Bansil, D. Grauer, Y. S. Hor, R. J. Cava, and M. Z. Hasan, Nat. Phys. **5**, 398 (2009).
[4] Z. Wang, Y. Sun, X. Q. Chen, C. Franchini, G. Xu, H. Weng, X. Dai, and Z. Fang, Phys. Rev. B **85**, 195320 (2012).
[5] Z. Wang, H. Weng, Q. Wu, X. Dai, and Z. Fang, Phys. Rev. B **88**, 125427 (2013).
[6] H. Weng, C. Fang, Z. Fang, B. A. Bernevig, and X. Dai, Phys. Rev. X **5**, 011029 (2015).
[7] S.-M. Huang, S.-Y. Xu, I. Belopolski, C.-C. Lee, G. Chang, B. Wang, N. Alidoust, G. Bian, M. Neupane, C. Zhang, S. Jia, A. Bansil, H. Lin, and M. Z. Hasan, Nat. Commun. **6**, 7373 (2015).
[8] A. A. Soluyanov, D. Gresch, Z. Wang, Q. Wu, M. Troyer, X. Dai, and B. A. Bernevig, Nature (London) **527**, 495 (2015).
[9] H. Huang, S. Zhou, and W. Duan, Phys. Rev. B **94**, 121117(R) (2016).
[10] B. Q. Lv, T. Qian, and H. Ding, Rev. Mod. Phys. **93**, 025002 (2021).
[11] K. Deng, G. Wan, P. Deng, K. Zhang, S. Ding, E. Wang, M. Yan, H. Huang, H. Zhang, Z. Xu, J. Denlinger, A. Fedorov, H. Yang, W. Duan, H. Yao, Y. Wu, S. Fan, H. Zhang, X. Chen, and S. Zhou, Nat. Phys. **12**, 1105 (2016).
[12] X. Huang, L. Zhao, Y. Long, P. Wang, D. Chen, Z. Yang, H. Liang, M. Xue, H. Weng, Z. Fang, X. Dai, and G. Chen, Phys. Rev. X **5**, 031023 (2015).
[13] Y.-Y. Lv, J. Xu, S. Han, C. Zhang, Y. Han, J. Zhou, S.-H. Yao, X.-P. Liu, M.-H. Lu, H. Weng, Z. Xie, Y. B. Chen, J. Hu, Y.-F. Chen, and S. Zhu, Nat. Commun. **12**, 6437 (2021).
[14] M. Hirayama, R. Okugawa, S. Ishibashi, S. Murakami, and T. Miyake, Phys. Rev. Lett. **114**, 206401 (2015).
[15] K. Nakayama, M. Kuno, K. Yamauchi, S. Souma, K. Sugawara, T. Oguchi, T. Sato, and T. Takahashi, Phys. Rev. B **95**, 125204 (2017).
[16] M. Sakano, M. Hirayama, T. Takahashi, S. Akebi, M. Nakayama, K. Kuroda, K. Taguchi, T. Yoshikawa, K. Miyamoto, T. Okuda, K. Ono, H. Kumigashira, T. Ideue, Y. Iwasa, N. Mitsuishi, K. Ishizaka, S. Shin, T. Miyake, S. Murakami, T. Sasagawa, and Takeshi Kondo, Phys. Rev. Lett. **124**, 136404 (2020).
[17] G. Gatti, D. Gosálbez-Martínez, S. S. Tsirkin, M. Fanciulli, M. Puppin, S. Polishchuk, S. Moser, L. Testa, E. Martino, S. Roth, Ph. Bugnon, L. Moreschini, A. Bostwick, C. Jozwiak, E.

Rotenberg, G. Di Santo, L. Petaccia, I. Vobornik, J. Fujii, J. Wong, D. Jariwala, H. A. Atwater, H. M. Rønnow, M. Chergui, O. V. Yazyev, M. Grioni, and A. Crepaldi, Phys. Rev. Lett. **125**, 216402 (2020).

[18] N. Zhang, G. Zhao, L. Li, and C.-G. Zeng, Proc. Natl Acad. Sci. USA **117**, 11337 (2020).

[19] J. Chen, T. Zhang, J. Wang, L. Xu, Z. Lin, J. Liu, C. Wang, N. Zhang, S. P. Lau, W. Zhang, M. Chhowalla, and Y. Chai, Sci. Adv. **8**, eabn3837 (2022).

[20] G. Qiu, C. Niu, Y. Wang, M. Si, Z. Zhang, W. Wu, and P. D. Ye, Nat. Nanotechnol. **15**, 585 (2020).

[21] N. Zhang, B. Cheng, H. Li, L. Li, and C.-G. Zeng, Chin. Phys. B **30**, 087304 (2021).

[22] C. Şahin, J. Rou, J. Ma, and D. A. Pesin, Phys. Rev. B **97**, 205206 (2018).

[23] G. P. Maruggi, J. Ferreira, E. Baggio-Saitovitch, C. Enderlein, and M. B. Silva Neto, Phys. Rev. Mater. **7**, 014204 (2023).

[24] F. Calavalle, M. Suárez-Rodríguez, B. Martín-García, A. Johansson, D. C. Vaz, H. Yang, I. V. Maznichenko, S. Ostanin, A. Mateo-Alonso, A. Chuvilin, I. Mertig, M. Gobbi, F. Casanova, and L. E. Hueso, Nat. Mater. **21**, 526 (2022).

[25] C. Niu, G. Qiu, Y. Wang, Z. Zhang, M. Si, W. Wu, and P. D. Ye, Phys. Rev. B **101**, 205414 (2020).

[26] T. Ideue, M. Hirayama, H. Taiko, T. Takahashi, M. Murase, T. Miyake, S. Murakami, T. Sasagawa, and Y. Iwasa, Proc. Natl Acad. Sci. USA **116**, 25530 (2019).

[27] G. Kresse and J. Furthmüller, Comput. Mater. Sci. **6**, 15 (1996).

[28] G. Kresse and J. Furthmüller, Phys. Rev. B **54**, 11169 (1996).

[29] P. E. Blöchl, Phys. Rev. B **50**, 17953 (1994).

[30] G. Kresse and D. Joubert, Phys. Rev. B **59**, 1758 (1999).

[31] J. P. Perdew, A. Ruzsinszky, G. I. Csonka, O. A. Vydrov, G. E. Scuseria, L. A. Constantin, X. Zhou, and K. Burke, Phys. Rev. Lett. **100**, 136406 (2008).

[32] C. Adenis, V. Langer, and O. Lindqvist, Acta Cryst. C **45**, 941 (1989).

[33] H. Peng, N. Kioussis, and G. J. Snyder, Phys. Rev. B **89**, 195206 (2014).

[34] S.-S. Chen, Y.-Cheng Luo, Y.-Y. Zhang, S.-T. Dong, Y.-Y. Lv, Y.-S. Cui, S.-H. Yao, J. Zhou, and Y. B. Chen, J. Appl. Phys. **126**, 055108 (2019).

[35] S. J. Blundell, *Magnetism in Condensed Matter* (Oxford University Press, New York, 2001).

[36] C.-L. Zhang, S.-Y. Xu, I. Belopolski, Z. Yuan, Z. Lin, B. Tong, G. Bian, N. Alidoust, C.-C. Lee, S.-M. Huang, T.-R. Chang, G. Chang, C.-H. Hsu, H.-T. Jeng, M. Neupane, D. S. Sanchez, H. Zheng, J. Wang, H. Lin, C. Zhang, H.-Z. Lu, S.-Q. Shen, T. Neupert, M. Z. Hasan, and S. Jia, Nat. Commun. **7**, 10735 (2016).

[37] X. Dai, H. Z. Lu, S. Q. Shen, and H. Yao, Phys. Rev. B **93**, 161110(R) (2016).

[38] B. L. Altshuler, A. G. Aronov, and D. E. Khmelnitsky, J. Phys. C: Solid State Phys. **15**, 7367 (1982).

[39] See Supplemental Material at http://link.aps.org/supplemental/10.1103/PhysRevB.108.195121 for details of the MR data and corresponding fitting results of samples S1-S4 at different T and θ, the comparisons between the first-principles calculation results of electronic-band-structure and the fitting results around the Weyl point by using effective Hamiltonian of equation (7) at the main text.

[40] B. N. Narozhny, G. Zala, and I. L. Aleiner, Phys. Rev. B **65**, 180202(R) (2002).

[41] Q. Li, D. E. Kharzeev, C. Zhang, Y. Huang, I. Pletikosić, A. V. Fedorov, R. D. Zhong, J. A. Schneeloch, G. D. Gu, and T. Valla, Nat. Phys. **12**, 550 (2016).

[42] B. I. Shklovskii and Alex L. Efros, *Electronic Properties of Doped Semiconductors* (Springer-Verlag Berlin, Heidelberg, 1984).

[43] M. V. Sadovskii, *Diagrammatics: Lectures on Selected Problems in Condensed Matter Theory* (Russian Academy of Sciences, Moscow, 2006).

[44] Z. Ren, A. A. Taskin, S. Sasaki, K. Segawa, and Yoichi Ando, Phys. Rev. B **82**, 241306(R) (2010).

[45] T. O. Wehling, A. M. Black-Schaffer, and A. V. Balatsky, Adv. Phys. **63**, 1 (2014).

[46] Y. Wang, E. Liu, H. Liu, Y. Pan, L. Zhang, J. Zeng, Y. Fu, M. Wang, K. Xu, Z. Huang, Z. Wang, H.-Z. Lu, D. Xing, B. Wang, X. Wan, and F. Miao, Nat. Commun. **7**, 13142 (2016).

[47] Y. Y. Lv, Xiao Li, B.-B. Zhang, W. Y. Deng, S.-H. Yao, Y. B. Chen, J. Zhou, S.-T. Zhang, M.-H. Lu, L. Zhang, M. Tian, L. Sheng, and Y.-F. Chen, Phys. Rev. Lett. **118**, 096603 (2017).

[48] H.-Z. Lu and S.-Q. Shen, Front. Phys. **12**, 127201 (2017).

[49] T. Ando, T. Nakanishi, and R. Saito, J. Phys. Soc. Jpn. **67**, 2857 (1998).